Phys Chem Minerals (2006) 33: 45–62
DOI 10.1007/s00269-005-0056-8

ORIGINAL PAPER

Anne M. Hofmeister

Thermal diffusivity of garnets at high temperature

Received: 1 June 2005 / Accepted: 15 November 2005 / Published online: 13 January 2006

Abstract Thermal diffusivity (D) of garnets with diverse chemical compositions was measured using the laser-flash technique, which is accurate ($\pm 2\%$) and isolates the lattice component from direct radiative transfer. Temperatures ranged from ~290 to ~1,600 K (unless limited by melting). Seven synthetic (e.g., YAG, GGG) and 15 natural garnets with two types of ionic substitution [$Ca_3(Fe,Al)_2Si_3O_{12}$ and $(Mg,Fe,Ca)_3Al_2Si_3O_{12}$] and varying amounts of OH^- were examined. Cation substitution or hydroxyl incorporation lowers D from end-member values. Thermal diffusivity is constant once the temperature (T) exceeds a critical value (T_{sat}) of ~1,100 to 1,500 K. From ~290 K to T_{sat}, the measurements are best represented by $1/D = A + BT + CT^2$ where A, B, and C are constants. These constants vary little among diverse chemical compositions, suggesting that the oxygen sublattice controls heat transport. Higher order terms are needed only when T_{sat} is low, such as Ant Hill garnet wherein $1/D = 0.049403 + 0.0032299T - 2.3992T^2\times10^{-6} + 6.0168T^3\times10^{-10}$ ($1/D$ in s/mm^2; T in K). The mean free path (λ, computed from D and sound velocities) is slightly larger than the lattice parameter above T_{sat}, in accord with phonon–phonon interactions requiring non-localized modes. At most temperatures, λ is nm-sized. Large values of λ are obtained by extrapolation to a few Kelvins, suggesting that boundary scattering can only be important at extremely cold temperatures. The observed behavior with T and chemical composition is consistent with the damped harmonic oscillator model. Phonon transport is best represented by inverse thermal diffusivity wherein $1/D$ goes as T^n where n is between 1 and 3 up to ~200 K, depends on a quadratic or cubic polynomial at moderate T, but is constant above T_{sat}. The predicted and observed temperature response of $1/D$ mimics the well-known form for heat capacity, in that acoustic modes control heat transport near cryogenic temperatures, optic phonons dominate above ambient temperature, and a limit analogous to that of Dulong and Petit is reached at very high temperature, due to full population of discrete phonon states.

Keywords Garnet · Thermal diffusivity · High temperature · Laser-flash technique · Disorder

A. M. Hofmeister (✉)
Department of Earth and Planetary Sciences, Washington U, 1 Brookings Dr, St Louis, MO, 63130-4899 USA
E-mail: hofmeist@wustl.edu
Tel.: +1-314-9357440
Fax: +1-314-9357361

Introduction

Measurements of thermal conductivity (k) and its close relative, thermal diffusivity:

$$D = \frac{k}{\rho C_P}, \quad (1)$$

where ρ is density and C_P is heat capacity at constant pressure (P), provide insight into microscopic behavior of solids, and find use in various applications. For example, numerical convection models of Earth's mantle have shown that the functional form for $k(T)$ strongly influences the character of the solutions and, thus, accurately characterizing $k(T)$ or $D(T)$ is essential to modeling planetary heat flow (e.g., Gerbault 2000; Branlund et al. 2000; Dubuffet et al. 2002; van den Berg et al. 2004; Yanagawa et al. 2005). Two different microscopic processes pertain. Transport of heat by scattering of phonons within each individual mineral grain is termed lattice conductivity (k_{lat}). Heat is also moved when photons emitted by any given grain in the medium are absorbed by nearby grains. This diffusive radiative process is described by an effective thermal conductivity ($k_{rad,dif}$), see e.g., Hofmeister (2004a, 2005).

Many geological studies of $k(T)$ or $D(T)$ utilize contact techniques such as Ångström's method, which has a nominal accuracy of ~5%, but interlaboratory discrepancies of ~20 to 30% (Ross et al. 1984). Data

on silicates and oxides are often problematic, being affected by direct radiative transfer above ~800 K, as indicated by the reversal of the sign of $\partial k/\partial T$ from negative to positive near this temperature (e.g., Kanamori et al. 1968). In direct radiative transfer, photons from the source either heat the opposite side of the sample or directly warm the sensor without participation of the sample. This process occurs when some spectral segment in the near-IR to visible is transparent, and, in contrast to diffusive radiative transport, is not a physical property since it depends on external variables such as the coatings used for thermal contact. This process is irrelevant to geophysics. Contact methods do not permit separation of radiative from phonon processes, are subject to errors associated with thermal contact resistance and differential thermal expansion, and are limited to $T < 1{,}200$ K (e.g., Parker et al. 1961). Transient techniques allow separation of vibrational from radiative effects but were only recently applied to Earth materials (e.g., Buettner et al. 1998; Schilling 1999; Höfer and Schilling 2002; Hofmeister 2004b).

Few heat transport studies exist of garnets, despite their geological and technological importance. Measurements were made of D or k_{lat} from ~298 to ~1,000 K for synthetic gallium garnets (Petrunin et al. 1989) and four natural garnets with similar chemical compositions (Kanamori et al. 1968; Osako 1997; Osako et al. 2004), and below 298 K for diverse synthetic and five natural garnets (Slack and Oliver 1971). Additional measurements exist near 298 K (e.g., Horai 1971), but few report chemical compositions.

The present study uses the laser-flash technique (Parker et al. 1961; Buettner et al. 1998) to isolate and accurately measure the lattice contribution to $D(T)$ of 22 chemically distinct garnets. Advantages of our method are that neither heat input nor the absolute temperature need be quantified. Instead, thermal diffusivity is derived from measurements of relative temperature, time, and sample thickness, all of which can be accurately determined, leading to uncertainties in D of 2% (Blumm and Opfermann 2002), largely resulting from uncertainties in sample thickness. The method is related to that of Shilling (1999) and Höfer and Schilling (2002), but differs in that higher temperatures are accessed, short laser pulses are used, thermocouples are avoided, and direct radiative transfer is quantified and removed after Mehling et al. (1998).

The goal is to use the accuracy and extended temperature range of our measurements to establish the functional dependence of D_{lat} on T, which can be used in geodynamic studies, and to probe microscopic behavior. Models for the temperature dependence of k_{lat} and D are evaluated through comparison with these new data, as well as with previous cryogenic measurements (Slack and Oliver 1971) to better understand heat transport. Because the remainder of this report concerns phonon processes, the subscript denoting the lattice contribution is omitted.

Theory of heat transport in non-metallic solids

Debye's (1914) analogy of the scattering of phonons to collisions of molecules in a gas is the basis of all models of heat transport in insulators. Debye's result is:

$$k = \frac{\rho}{3ZM} C_V u^2 \tau \tag{2}$$

where M is the molar formula weight, Z is the number of formula units in the primitive unit cell, τ is the mean free lifetime, and u is an acoustic velocity. Parameters for acoustic modes have generally been used to calculate k, but with limited accuracy because lifetimes are roughly estimated (e.g., Ziman 1962). An alternative (optic) model was developed to address this problem (Hofmeister 1999, 2001, 2004b; Giesting and Hofmeister 2002). These papers focus on k at 298 K, whereas the present paper centers on $D(T)$.

Acoustic models for the temperature dependencies of k and D

By assuming three phonon collisions and that the mean free path ($\lambda = u\tau$) goes as $1/T$ above the Debye temperature (θ), Peierls (1929) reproduced Euken's (1911) empirical law:

$$k = \frac{B}{T} \text{ for } T > \theta. \tag{3}$$

Equation 3 should hold up to the melting point of most solids, including minerals (Liebfried and Schlomann 1954; Roufosse and Klemens 1974). For four-phonon events and $\lambda \sim 1/T$, Pomeranchuk (1943) obtained $k \sim T^{-5/4}$. Klemens (1969) proposed the form:

$$k \sim \frac{1}{BT + CT^2}\ , \tag{4}$$

similarly, Ziman (1962) suggested that:

$$k \sim \frac{1}{BT} + \frac{1}{CT^2}\ . \tag{5}$$

If defect (e.g., chemical substitutions) concentrations exceed 5 atom %, models predict:

$$k = B/T^n \text{ where } 0 < n < 1 \tag{6}$$

(Roufosse and Klemens 1974). Scattering from defects and vacancies has also been used to justify a formula widely applied to rocks:

$$k \sim \frac{1}{\mathrm{A} + \mathrm{B}T} \text{ for } T > \theta \tag{7}$$

(Madarsz and Klemens 1987; Siepold 1998).

Equations 3, 4, 5, 6, and 7 are high temperature limits. Because heat capacity is nearly constant for $T > \theta$, forms identical to Eqs. 3, 4, 5, 6, and 7 are expected for D.

At ordinary temperatures, k is roughly approximated by:

$$k \sim \exp(-\theta/T) \quad \text{for } T<\theta \tag{8}$$

(Ziman 1962). Other similar forms can be found in the literature.

An optic model for the temperature dependence of D

Lifetimes in Eq. 2 are extracted from IR spectra using the damped harmonic oscillator (DHO) model of Lorentz. For each mode, $\tau_i = 1/2\pi\text{FWHM}_i$, where FWHM is the full width at half maximum of peaks in the dielectric function (e.g., Spitzer et al. 1962). For any given mode, FWHM_i describes its interaction with all other modes in a real crystal, and thus includes effects such as harmonicity, disorder and impurities. Generally, FWHM_i and acoustic velocities are averaged (e.g., Hofmeister 2001, 2004b, c). From Eq. 2, the above information, and neglecting the small, ~3% difference between C_P and C_V, provides the new formula:

$$D(T) = \frac{\langle u(T)\rangle^2}{6\pi Z\langle \text{FWHM}(T)\rangle} = \frac{\langle u(T)\rangle\langle \lambda(T)\rangle}{3Z}. \tag{9}$$

Sound velocities of dense minerals depend weakly on temperature. For grossular and pyrope garnets, $\partial(\ln u)/\partial T \sim -0.004\%/\text{K}$ (Anderson and Isaak 1995). IR reflectivity at temperature are unavailable for garnets. Although Raman spectra show that garnet peak widths increase strongly with T (Gillet et al. 1992), values were not reported. Quantitative IR data for MgO reveal extremely large derivatives for dielectric peak widths: $\partial(\ln \text{FWHM})/\partial T = 0.25\%/\text{K}$ (Kachare et al. 1972). Equation 9, the strong dependence of FWHM on T, weak changes of u with T, and FWHM being finite at 4 K for MgO (Kachare et al. 1972) lead to:

$$\begin{aligned}\frac{1}{D} &= \frac{6\pi Z}{u_0^2}(\text{FWHM}_0 + aT + \ldots)(1 + bT + \ldots) \\ &\approx A + BT + CT^2 + \ldots\end{aligned} \tag{10}$$

where a, A, etc. are constants. The linear coefficient B should dominate and has a positive sign.

Low temperature limits

Acoustic models assume that $1/\lambda \sim T$. At low temperature, heat capacity generally goes as T^3. Density and sound speeds are finite, and thus negligibly affect D in the limit $T \to 0$. Consequently, $k \sim T^2$ and $D \sim 1/T$ in the limit $T \to 0$. Scattering from grain boundaries or sides of the sample provides a mean free path (λ_2) that is independent of temperature (e.g., Ziman 1962). Using $1/\lambda_{\text{tot}} = 1/\lambda_1 + 1/\lambda_2$ gives constant D as $T \to 0$, and $k \sim T^3$.

The optic model provides similar forms near 0 K. If $<\text{FWHM}>$ is finite as $T \to 0$, then $1/D \sim$constant, and $k \sim T^3$ as $T \to 0$. If instead, FWHM $\to 0$ as $T \to 0$, then $D \sim 1/T$ and $k \sim T^2$ at low temperature. Allowing for intermediate cases provides the general result:

$$D = \frac{D_0}{T^m},\ 0<m<1. \tag{11}$$

Experimental methods

Samples and their characteristics

Five synthetic end-member single-crystals, two doped synthetic gallium garnets, and 15 natural garnets were studied. The main criterion in selecting samples was large size, although four samples are at the minimum size requirement of 6 mm, marked "small" in Table 1. Most of the natural samples have fractures or inclusions, but five were flawless single-crystals. Six of the natural samples have chemical compositions that are close to one of the garnet binaries, whereas two are nearly end-members (Table 1). Samples were given labels such as Py–Al, in accord with the dominant components and whether the sample is binary or not. Ant Hill and xenocryst samples are derived from shallow mantle beneath the Colorado plateau (Schaal 1991). Similar samples from this provenance originated at 950–1,230°C and 3.2–4 GPa (Ehrenberg 1982).

Sample preparation

Samples were shaped into plates with parallel surfaces and doubly polished. Thickness is 0.6–2.0 mm and diameters are mostly 8–15 mm (Table 1). After electron microprobe analyses or spectroscopic measurements were performed, the sample was sandblasted with alumina of ~100 μm grit size, and then thickness was measured using a calibrated binocular microscope and crosschecked with a micrometer. Most samples were sputter-coated with Pt using a Quorum Technologies SC-7620 mini-sputter coater. This step was omitted for dark samples (YIG, andradite, and An–Gr), small samples where runs were limited to low temperatures (xenocryst, NdGG, Gr–An2, Mn-rich Gr), and strongly colored SmGG:Fe and EuGG crystals. SmGG was run with and without an Au–Pd coat. All samples were top-coated with commercially available graphite spray. Coatings were sufficiently thick to suppress direct radiative transfer at 298 K, and to reduce direct radiative transfer at elevated temperatures.

Electron microprobe analysis

Wavelength dispersive analyses were obtained using a JEOL-733 electron microprobe equipped with Advanced Microbeam™ automation. The accelerating voltage was 15 kV, the beam current was nominally 30 nA, and the

Table 1 Sample characteristics

Name	Location	Composition						Key	No.[a]	Source	Description-before runs	Description-after runs
		Py	Al	Sp	Gr	An	Uv					
Xenocryst[e]	Garnet Ridge, Az	75	15	0	12	0	2		5[b]	R. Schaal, EGR4x	Red-purple single-crystal 5×7 mm^2 "D" shape	Unchanged
Rhodolite	Madagascar	56.0	37.9	0.8	5.3	0	0	g	40	Unknown	Purple-red single-crystal with tiny inclusions	Cloudy, extremely fractured
Py–Al	Unknown	43	52	1	4	0	0		36[b]	W.C. Metropolis, Harvard 129076	Purple-red single-crystal	Melted during final run
Ternary	Gore Mt., NY	39.4	48.8	1.3	10.6	0	0	h	16	Washington U.	Red-orange single-crystal, fractured	More fractures
Ant Hill	Garnet Ridge, AZ	35.0	43.5	1.7	19.8	0	0	f	4–9	R. Schaal, WGR1G	Red single-crystal	Melted during final run
Al–Gr	Potato Hill, Newfoundland	5	72	3	17	0	3		47[b]	J.V. Owen VO-87-041A	Dark red, fractured	More fractures
Al–3;-Py	Ft. Wrangle, AK	21.1	72.7	1.6	4.6	0	0	i	17	Excaliber	Red, fractured	Melted
Al–Sp	Yamano, Japan	1	61	37	1	0	0		39[b]	W.C. Metropolis, Harvard 104623	Orange-red single-crystal	Melted
Sp-rich	Haddam, CT	5.1	15.7	60.9	18.3	0	0	j	–-	Excaliber	Orange polycrystal fractured	Melted
Grossular	Asbestos, Quebec	0	1.3	0.1	95.6	3.0	0	k	B12	Excaliber	Pale orange single-crystal; 2nd piece was wetter	Melted; 2nd piece slightly cloudy
Gr–Mn-rich[e]	Sierra de las Cruces, Caohuila, Mexico	3	0	0	89.3	2.4	5.3[d]	d		Schooler's	Pink, grading lighter inwards, Cloudy, 6 mm octahedron	Unchanged
Gr–An	Lake Jaco, Mexico	3.0	0	0.0	85.6	11.0	0.1		B36[b]	U. C. Davis	Yellow-green single-crystal, few fractures	More fractures, cloudy
Gr–An 2	Unknown	0.6	1.6	0.4	79.3	18.1	0	l	B45	U.C. Davis	Honey-color single-crystal, fractures, 5.5×9 mm^2	Unchanged
An–Gr	Garnet Hill, Calavaras Co.,CA	0	3	5	15	77	0	m	B35	A Kampf LA Co. Nat. Hist.	Dark red (rim of sample), many fractures	Unchanged
Andradite	Stanley Butte, AZ	0.1	0	0.3	1.0	98.4	0.1		B43[b]	J de Mouth, Cal. Acad. Sci.	Brown-green crystal, fractures rim is darker	Unchanged
YAG	Synthetic	$Y_3Al_5O_{12}$							c	Morion Co.	Colorless single-crystal	Amber after highest T run, coating baked on
YIG	Synthetic	$Y_3Fe_5O_{12}$							c	Morion Co.	Black single-crystal	Unchanged
NdGG	Synthetic	$Nd_3Ga_5O_{12}$							–-	Atomergic	Pink single-crystal 5×5 mm^2 square	Unchanged
SmGG	Synthetic	$Sm_3Ga_5O_{12}$							–-	Morion Co.	Yellow single-crystal	Unchanged
SmGG:Fe	Synthetic	$Sm_3Ga_5O_{12}$ doped with Fe							–-	Morion Co.	Amber single-crystal	Unchanged
EuGG:Cr	Synthetic	$Eu_3Ga_5O_{12}$ doped with Cr							–-	Morion Co.	Bright green single-crystal	Unchanged
GGG	Synthetic	$Gd_3Ga_5O_{12}$							–-	Morion Co.	Colorless single-crystal	Brown after highest T run

[a]Index numbers are for similar samples described in Hofmeister et al. (1998) and referenced to earlier literature. For grossular–andradites, index numbers and detailed description are in McAloon and Hofmeister (1995) End-members are *Py* pyrope ($Mg_3Al_2Si_3O_{12}$), *Al* almandine ($Fe_3Al_2Si_3O_{12}$), *Sp* spessartine ($Mn_3Al_2Si_3O_{12}$), *Gr* grossular ($Ca_3Al_2Si_3O_{12}$), *An* andradite ($Ca_3Fe_2Si_3O_{12}$), and *Uv* uvarovite ($Ca_3Cr_2Si_3O_{12}$)

[b]Indicates that the same sample was used for IR measurements (McAloon and Hofmeister 1995; Hofmeister et al. 1996): microprobe analyses were taken from the above listed studies

[c]Spectral data in Hofmeister and Campbell (1992), revised by Geisting and Hofmeister (2002)

[d]Recalculated analysis of Geiger et al. (1999). This sample has unusual chemistry; instead of uvarovite, the component is $Ca_3Mn_2Si_4O_{12}$

[e]Small sample

[f]$N = 21$; Py content varies from 37.6 to 41.4%; ranges for other components are similar

[g]$N = 10$, Py content varies from 55.4 to 56.1%; ranges for other components are similar

[h]A second chip was examined; $N = 10$, Py content varies from 38.6 to 41.4%

[i]$N = 16$, Py content varies from 19.8 to 21.9%, ranges for other components are similar

[j]$N = 15$, Py content varies from 4.4 to 5.6%; ranges for other components are similar

[k]$N = 2$, negligible variation

[l]$N = 16$, Gr content varies from 78 to 81%, ranges for other components are similar

[m]$N = 5$, little variation

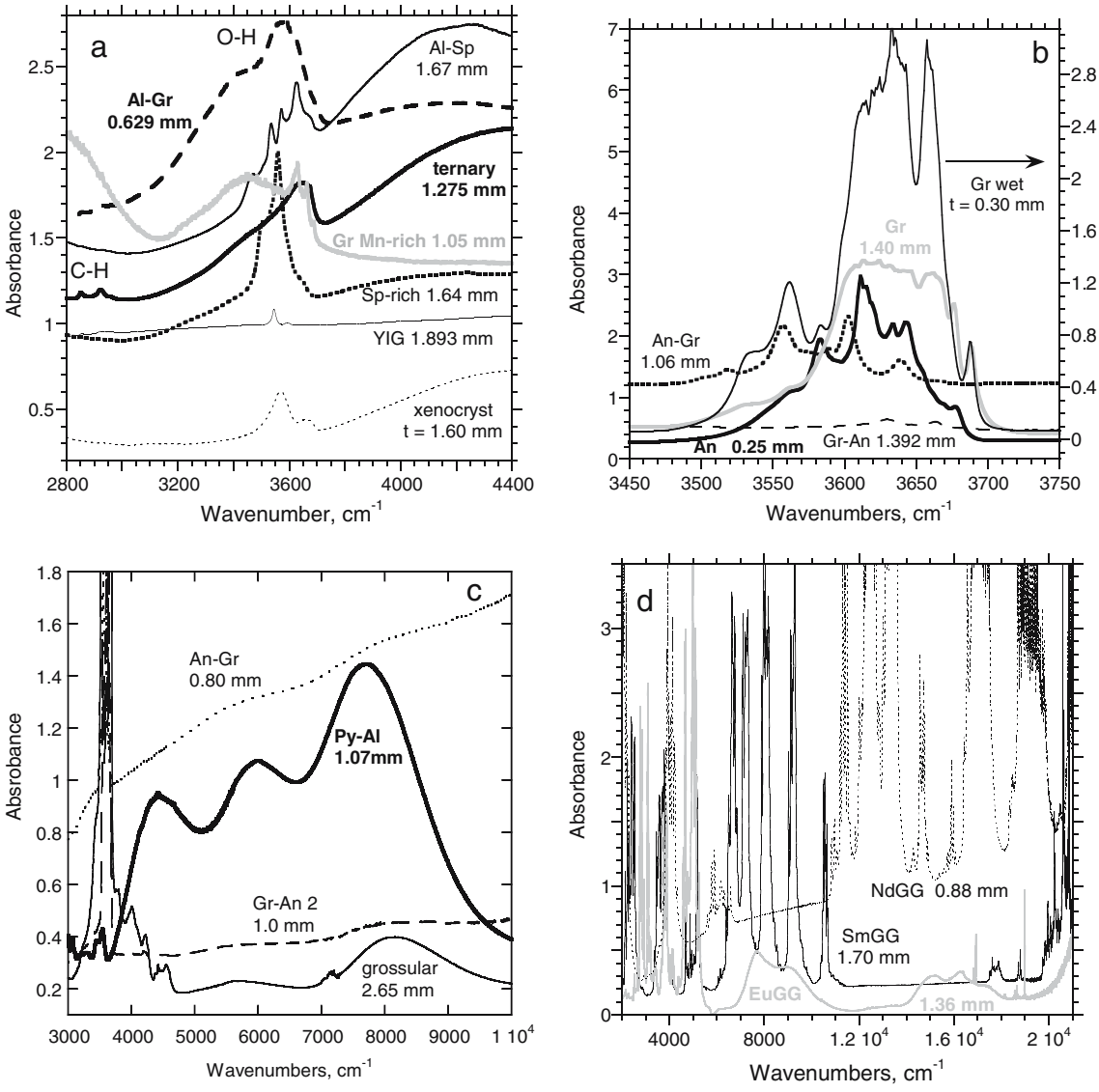

Fig. 1 Near-IR spectra of representative samples. Curves with various patterns are labeled with sample names from Table 1 and thickness. Spectra are uncorrected for baselines. **a** O–H region for pyrope, almandine, spessartine, and YIG garnets. Mn-rich grossular is shown here to depict its broad H_2O band. C–H = hydrocarbon deposits. The broad band near 4,200 cm^{-1} is due to Fe^{2+} in the dodecahedral site. The rise towards low ν is due to the strong first overtone of the Si–O stretching mode. **b** O–H region of grossular–andradites. The O–H bands occupy a narrow spectral range and are sharp. The Gr spectrum is distorted due to being overly thick. To compute OH content, Gr-wet was used as a proxy from 3,550 to 3,650 cm^{-1}, with thickness appropriately scaled. **c** Fe^{2+} region. Grossular–andradites with absorption bands in this region are compared to a pyrope–almandine with 52 mole% almandine. **d** Near-IR to visible region of the rare earth garnets. The spectrum of SmGG:Fe (not shown) is identical to that of SmGG

beam diameter was 1 μm for all spots. Silicates were used as standards. X-ray matrix corrections were based on a modified Armstrong (1988) CITZAF routine. Chemical composition is reported in terms of end-members (Table 1).

Spectroscopic analysis of hydroxyl and Fe^{2+} contents

Near-IR spectra were obtained using an evacuated Bomem DA3.02 Fourier transform interferometer with a SiC globar source, a liquid N_2 cooled InSb detector, and a CaF_2 beamsplitter. About 2,000 scans were collected from ~1,800 to 8,000 cm^{-1} at a resolution of 2 cm^{-1}. A quartz lamp and beamsplitter provided the range ~3,500 to 13,000 cm^{-1}. A Si-avalanche detector was used at a resolution of 4 cm^{-1} over ~9,000 to 22,000 cm^{-1}. Absorbance was calculated from:

$$a = -\log(I_{tra}/I_0). \quad (12)$$

For nearly end-member grossular and andradite, hydroxyl contents were obtained using:

$$H_2O\,wt\% = 0.0000786\,IA, \quad (13)$$

Table 2 Properties at ambient temperature (298 K) and comparison with literature values

Sample	H_2O[b] (ppm)	D (mm^2/s)	Previous D measurement						Previous k measurement	
			D (mm^2/s)	Py–Al–Gr–An[d]	ρ^{ε} (g/cm^3)	C_P^e (J/mol-K)	M^e (g/mol)	k (W/m-K)	k (W/m-K)	Py-Al-Gr-An[d]
Xenocryst[a, h]	22	1.27	1.06[i]	51–33–16–0	3.74	331	430	3.66	3.18[o]	c
Rhodolite	Bld	1.22	1.11[j]	60–40	3.86	332.8	441.93	3.55	4.5[p]	55-56-0-0
Py–Al[a]	Bld	1.43	1.09[j]	50–50	3.95	334.9	453.28	4.17	4.3[p]	49-51-0-0
Ternary	0-660	1.23	1.18[k]	34–58–8–0	3.93	334.5	452.81	3.56	3.31[o]	c
Ant Hill[a]	Bld	1.23	1.06[i]	51–33–16–0	3.89	334.6	455.1	3.52		
Al–Gr	5,000[s]	1.04	–		4.13	340.0	483.5	3.02	–	
Al–Py	Bld	1.25	1.19[l]	25–74–1–0	4.19	340.2	480.7	3.70	3.48[l]	25-74-1-0
Al–Sp[a]	440	1.55	–		4.18	341.8	495.3	4.47	–	
Sp-rich	830	1.18	–		3.95	338.3	482.9	3.26	3.39[o]	c
Gr[a]	2,700[f, t]	2.79	–		3.61	331.3	453.13	7.36	7.2[p]	0-4-96-0
Gr wet[a]	6,700[f]	2.50	–		3.61	331.3	453.13	6.60		
Gr Mn-rich[h]	7.2[g]	2.86			3.61	331.7	453.4	7.5		
Gr–An	120	2.83	–		3.64	331.5	454.2	7.51	~5.4[o]	"Grossular"
Gr–An 2[h]	155	2.77	–		3.66	334.2	461.4	7.34	–	
An–Gr	870	2.02	–		3.74	341.53	479.9	5.37	3.08[o]	0-0-30-70
An	5,900[f]	2.88	–		3.86	351.56	507.31	7.7	-	
YAG[a]	–	4.13	–		4.45	371.2	593.7	11.49	9.8[r], 10.3 [p], 13[q]	YAG
YIG[a]	15	2.17	7.1[m]	YIG	5.29	426.4	737.7	6.63	6[r], 7.4[p]	YIG
NdGG[h]	–	2.84	3.1[n]	NdGG	6.61	395	973	7.62	8.1[n]	NdGG
SmGG		2.14	–		6.86	~400	991	5.92	–	
SmGG:Fe		2.05	–		"	"	"	5.67	–	
EuGG:Cr		2.64	–		6.95	~402	996	7.40	–	
GGG[a]	–	1.93	2.8[n]	GGG	7.08	405	1012	7.94	7.5[n], 9.0[p]	GGG

[a]Single-crystal, no fractures, although the mantle sample has some inclusions of a darker red garnet
[b]Hydroxyl content is reported as H_2O because these species cannot always be distinguished
[c]Composition not reported, but this sample is from the same locality as our sample, and should have a similar composition
[d]Al includes Sp content
[e]After Giesting and Hofmeister (2002)
[f]OH^- contents obtained using the calibration of Rossman and Aines (1991); all others used that of Maldener et al. (2003)
[g]Also contains 59 ppm H_2O as fluid inclusions, [h]small sample
[i]Chai et al. (1996) their sample has more Fe and less Mg than ours
[j]Kanamori et al. (1968) The stated compositions are inconsistent with the reported cell constants and index of refraction, indicating that some Ca or Mn are substituted. See Giesting and Hofmeister (2002)
[k]Osako (1997), [l]Osako et al. (2004), [m]Bertolotti et al. (1988), [n]Petrunin et al. (1989), [o]Horai (1971). Compositions were not reported and are estimated from literature reports for the same locality, if available, [p]Slack and Oliver(1971), [q]Klein and Croft (1967), [r]Padture and Klemens (1997). D was measured for ceramic samples, but only k was reported
[s]Likely alteration in cracks, [t]Content estimated, see Fig. 2

where $IA = \int a(\nu)\mathrm{d}\nu/t$ is the integrated absorbance from ~3,450 to 3,730 cm^{-1} and t is thickness (Rossman and Aines 1991). For solid solution garnets, hydroxyl contents are approximated from

$$H_2O\,\mathrm{wt}\,\% = 1.8\,IA/(\rho\varepsilon) \quad (14)$$

where ρ is an average density of 3.7 g/cm^3 and ε is an average extinction coefficient of 3,630 L/mol-cm^2 (Maldener et al. 2003) which gives 1.6 times the amount of Eq. 13.

The various near-IR spectral patterns (Fig. 1) and associated OH^- contents (Table 2) are similar to previous results (e.g., Aines and Rossman 1984; Rossman and Aines 1991; Amthauer and Rossman 1998; Maldener et al. 2003). For the wet grossular, spectra collected before and after heating differ insignificantly (not shown). Mn-rich grossular lost fluid inclusion water (broad band in Fig. 1a), but its hydroxyl spectrum (sharp bands) was similarly unchanged. Hydroxyl contents of the remaining samples are unlikely to be affected by heating.

Broad bands from 3,500 to 10,000 cm^{-1} are associated with Fe^{2+} in the dodecahedral site (Fig. 1c), e.g. Taran and Langer (2001). Comparing absorption coefficients of the strongest Fe^{2+} band at 8,150 cm^{-1} in the grossular–andradites to that of Py–Al suggests that $Fe_3Al_2Si_4O_{12}$ contents are 3.7 mol% for both grossular and An–Gr, 2.7 wt% for Gr–An2, but negligible for the other grossular–andradites. Given that a low Ca garnet was used as a standard, and intensity, rather than peak area, was compared, these results are consistent with electron microprobe analysis (Table 1).

Absorption spectra of Fe-doped and pure SmGG differ negligibly (Fig. 1d), suggesting that the iron is ferric, since this absorbs above our frequency range. The absorption pattern of SmGG differs from those of Cr-doped EuGG and NdGG, but all have many sharp bands indicative of rare earth elements. Broad bands at

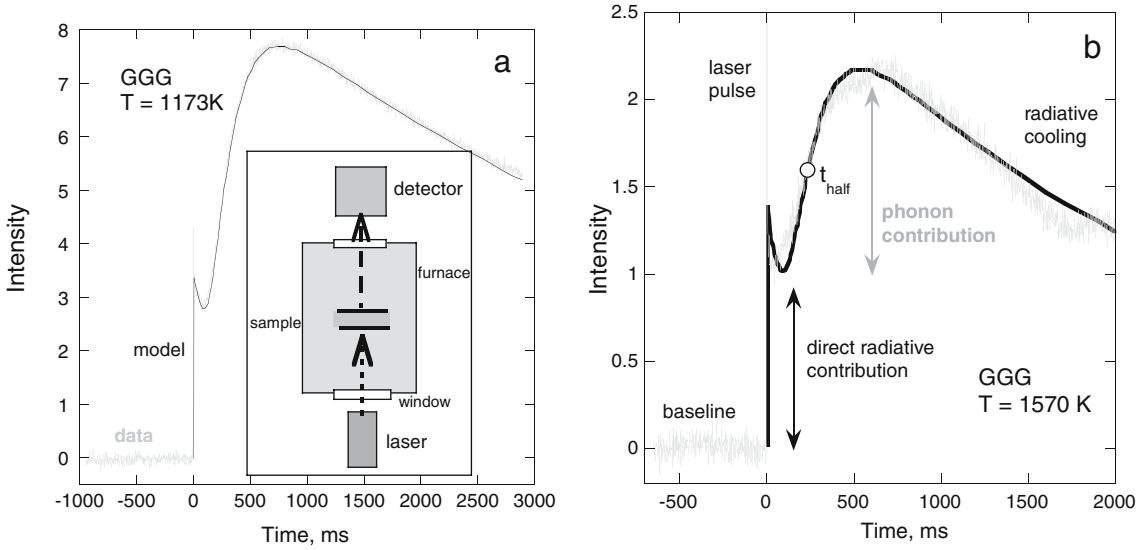

Fig. 2 Essentials of laser-flash measurements. Inset (in part **a**): schematic of instrument components. A sample disk (*gray with coated top and bottom*) of thickness L is held at temperature by the furnace. Emissions of the sample (*dashed arrow*) are monitored by an IR detector, providing a baseline, which is set to 0 intensity for convenience. A laser pulse (*dotted arrow*) heats the coated bottom of the sample (spike at 0 ms). As the heat diffuses from the bottom to the top of the sample, emissions increase to a maximum, and then the sample radiates heat to the surroundings until equilibrium is again attained. Larger section: temperature–time curves recording emissions of GGG. The *jagged light gray curve* is the data, whereas the *smooth heavy black line* is the fit. **a** Example of good data. **b** Example of a sample reaction, as indicated by the misfit of model to data. The half rise time (t_{half}, Eq. 15) is shown for illustrative purposes only as radiative transfer affects this temperature–time curve

16,000 and >21,000 cm^{-1} in Cr-doped EuGG are consistent with spectra of Cr^{3+} in a tetrahedral site, after Rossman (1988). Broad bands at ~7,700 and 9,000 cm^{-1} are assigned to Cr^{3+} in the octahedral site.

Laser-flash analysis

The Netzsch LFA 427 apparatus accesses temperatures from ~290 to 2,200 K under an argon atmosphere (for details see Braeuer et al. 1992; Blumm and Lemarchand 2002). The main components are an evacuable furnace with a graphite-heating element and water cooled housing, an Nd-GGG laser, and an InSb detector (Fig. 2).

Temperatures were monitored using a type D W/Re thermocouple placed near the sample, which was calibrated monthly against Curie transition points of Fe at 1,043 K and Co at 1,386 K. The Curie transition in YIG at 556 K and the α–β transition in quartz at 846 K provided crosschecks. Readings near ambient temperature were checked with a thermometer.

Thermal diffusivity values at temperature were calibrated against two standard reference materials from the National Institute of Standards and Technology (NIST): electrolytic iron (SRM-8421) and austenitic stainless steel (SRM-1460). Applying Cowan's (1963) model to our measurements produces D within 2% of (1) values obtained from 298 to 1,073 K on these specific materials using another laser-flash apparatus and of (2) D inferred from values of thermal conductivity at temperature obtained at NIST (Henderson et al. 1998a, b), thereby demonstrating that our instrument attains the nominal uncertainty attributed to this technique. Poco graphite, another SRM, was used as a secondary standard (Blumm and Lemarchand 2002).

In this fast, contact-free method, a sample in the form of a small slab with parallel faces is held at temperature in a furnace while emissions from the top of the slab are monitored remotely with an IR detector (Fig. 2). The bottom of the slab is heated by an optical pulse from the IR laser. As heat from the laser pulse diffuses from the bottom to the top of the sample, the increase in emissions is recorded by the IR detector, as a temperature–time curve (Fig. 2). Top and bottom surfaces of the sample are graphite-coated to enhance absorption of laser light while shielding the detector, and to increase the intensity of the IR emissions (e.g., Blumm et al. 1997). For the simplest case of adiabatic heating and no radiative heat losses from the surface:

$$D = \frac{0.1388\,L^2}{t_{\text{half}}}, \tag{15}$$

where L is the sample thickness and t_{half} is half of the time needed for the temperature to reach the maximum (Parker et al. 1961). The pulse must be shorter than the time it takes heat to cross the sample. Because the change in temperature across the sample associated with the pulse is small, ~4 K, D is approximately constant during data acquisition, and the temperature dependence of D is determined solely by varying furnace temperature (Parker et al. 1961).

Data were collected at intervals of 50–100 K as each garnet was heated to the maximum temperature. If the

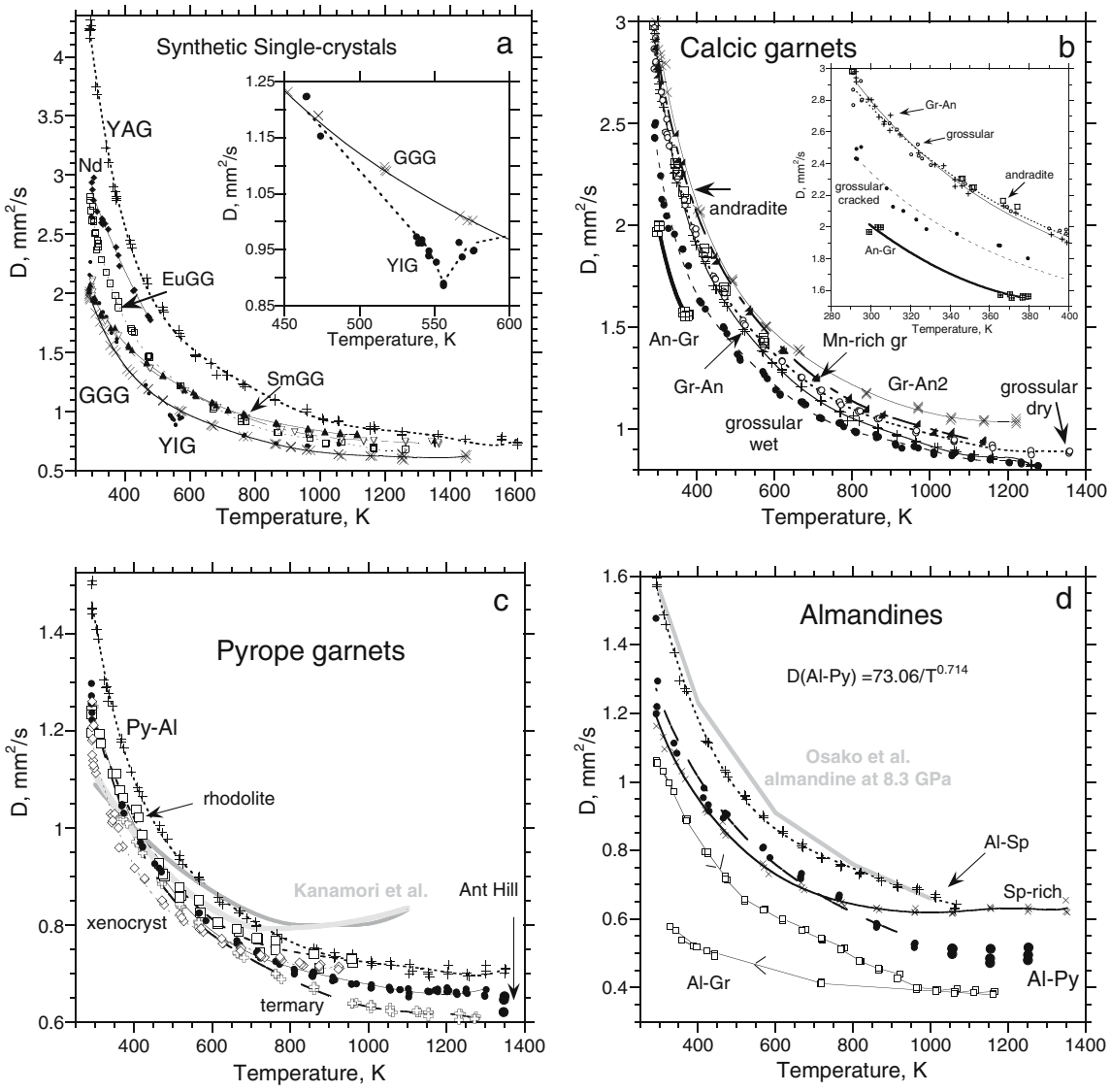

Fig. 3 Thermal diffusivity as a function of temperature. *Symbols* are labeled using the abbreviations in Table 1. Uncertainties of 2% are smaller than the symbols. **a** Single-crystal synthetic garnets. For GGG (*X*), the fit is a seventh order polynomial in temperature. For YAG (+), the fit is eighth order. *Filled diamonds* NdGG. *Open squares* EuGG. *Filled triangles* SmGG. *Open triangles* SmGG:Fe. *Inset* shows details of the ferromagnetic transition in YIG (*dots*) at 556 K. **b** Garnets with chemical compositions along the grossular–andradite binary. For the two grossulars (*circles*), Mn–grossular (*right triangles*) and Gr–An (+), the fits shown are seventh order polynomials in *T*. An–Gr is described by a quadratic polynomial. Andradite (*open square*) can be fit with a fourth order polynomial (not shown). Gr–An2 (*X*) is a very small sample. *Inset* shows a close up of the low-T behavior. **c** Pyrope-rich garnets. Polynomial fits are between fourth and sixth orders. Py–Al (+) is a flawless single-crystal; ternary (*open plus sign*) has few fractures. For Ant Hill garnet, only data below 1,300 K (*small dots*) were fitted: data at 1,300 K (*large dots*) are affected by partial melting. Problems in measuring rhodolite (*open square*) are discussed in the text. Xenocryst (*open diamonds*) was only graphite-coated and has some residual radiative transfer. *Light gray curve* $Py_{60}Al_{40}$ and *dark gray curve* $Py_{50}Al_{50}$ from Kanamori et al. (1968). **d** Almandine-rich garnets. Al–Sp (+) is a flawless single-crystal. Sp-ternary (*X*) and Al-Gr (*open square*) are highly fractured, and results at high-T are suspect, see text. Below 1,150 K, Al-Py (*filled circle*) was fit to a power law ($D = 69.44\ T^{-0.706}$). Comparison is made to Osako et al. (2004)

sample did not melt, data were collected during the cool down as well. Three measurements were made at each temperature step to provide reproducibility. Runs were repeated for most samples to ascertain reproducibility, to better constrain temperature regions where *D* changed rapidly, and to confirm the high temperature behavior of *D*. In some cases, experiments were run on two different slabs made from the same specimen.

To suppress (or at least reduce) direct radiative transfer, samples are coated with a highly reflective metal (Au–Pd or Pt) before applying graphite, after Degiovanni et al. (1994). Because direct radiative transfer is difficult to eliminate at high temperature, its effect on the temperature–time curves is incorporated in data analysis (Tan et al. 1991; Andre and Degiovanni 1995; Hofmann et al. 1997; Mehling et al. 1998).

Specifically, temperature–time curves were analyzed using software provided by Netzsch, which corrects for baseline drift during the measurement. The measured shape of the pulse was accounted for (Blumm and Opfermann 2002). The approach of Mehling et al. (1998) was used, which not only accounts for radiative losses at the surface and direct radiative transfer across the sample, but also allows for partial transparency [rather than using the T^3 law as did Schilling (1999) and Hofer and Schilling (2002), which assumes transparency at all frequencies]. Blumm et al. (1997) established model accuracy by comparing D calculated by applying Mehling et al.'s (1998) model to measurements of glass coated *with* graphite to D calculated by applying Cowan's (1963) model (which is closely related to Eq. 15) to measurements of the same glass, but with metal and C coatings.

The reliability of each data point was ensured by making it mandatory that the calculated and measured temperature–time curves match. Some misfits occurred at the highest temperatures in a given run (see Fig. 2), and result from either melting, chemical reaction of sample and coating, fracturing of the sample, or peeling of the Pt-C coating, as ascertained by examining the recovered sample. Problematic data are discarded, i.e., not included in fitting $D(T)$, although some of the problematic data are discussed in view of previous poor agreement among contact studies.

Results

General behavior

Thermal diffusivity of garnets decreases rapidly as temperature increases above ~290 K, such that the slope $\partial D/\partial T$ gradually decreases as T increases until D asymptotically approaches a constant at high temperature (Fig. 3). Shapes of the $D(T)$ curves vary among the samples, but garnets with similar chemical compositions have similar trends, e.g., GGG resembles YIG (Fig. 3a) and grossular resembles andradite (Fig. 3b). Little variation is seen among the pyrope-rich garnets (Fig. 3c), and $D(T)$ curves of almandines are roughly parallel (Fig. 3d).

Effect of fractures, inclusions, and reactions

Measurements of single-crystals are reproducible unless a chemical reaction occurred (YAG, GGG), or the sample shattered (rhodolite) or melted (e.g., grossular). Specifically, D values obtained at any given temperature during heating or cooling portions of a single run were indistinguishable, and/or values from multiple runs coincided. During the final runs of YAG and GGG to their maximum temperatures of 1,600 and 1,400 K, respectively, cooling curves differed from heating curves or from previous runs. The recovered YAG crystal had changed in color to amber, and the Pt coating had reacted with the surface. The GGG crystal had changed to black, probably due to reduction of rare earth ions. (The precise nature of the reactions is peripheral to the present study, and is relegated to future work.) Changes in the time–temperature curves (Fig. 2b) revealed exactly when such reactions occurred, and thus all affected data could be discarded.

For single-crystal rhodolite, a large amount of scatter exists among the three data points gathered at each temperature, such that the amount of scatter increased as T increased (Fig. 3c). Scatter in the datasets at a single temperature indicates non-uniform heating. After heating, the sample had fractured throughout. Unheated remnants of the original crystal had many, ~ micron-sized inclusions. Differential absorption of heat by the inclusions and garnet matrix would explain the presence of nonuniform heating which led to shattering. High temperature data from the rhodolite sample are excluded from the fits. The amount of scattering was used to determine the cut-off temperature.

Several samples melted (Table 1). This transition is evident in both temperature–time curves and the results, wherein D decreases during melting (Ant Hill garnet, Fig. 3c). Due to changes in sample thickness, partial melting, and/or intermixing with Pt and C coatings, D may not represent garnet melts and is not reported.

A few fractures or cracks existing in the sample prior to heating does not seem to affect measurements at low temperatures in that the initial slopes are consistent with that determined from single-crystals with similar compositions (Fig. 3b, c, d; Table 1). A fracture is a plane between two crystals, and heat is impeded by loss of contact across this plane. For most samples, the fractures are few and parallel to the flow of heat, and thus should affect thermal diffusivity very little. However, the trends in D with T above ~500 K diverge for Al–Gr and the spessartine-rich sample (Fig. 3d). Both samples are heavily fractured, and it is likely that the coatings seeped into the samples, or differential expansion between the grains occurred. Because Pt and C have higher thermal diffusivity than garnet, infiltration will increase the apparent D, whereas loss of contact should decrease the apparent D. Both types of behavior are seen for these samples, and these effects may exist simultaneously. Data with obvious problems were omitted from analysis.

In summary, intrinsic behavior, wherein D changes simply in response to temperature, is indicated by reproducible runs. In addition, intrinsic behavior can be distinguished from results affected by processes such as melting or redox reactions through the temperature–time curves. Such problematic data were omitted from further analysis. Data below ~500 K seem unaffected.

Size limitations

For diameters of 5–6 mm (e.g., xenocryst), room temperature data were deemed reliable as the same D values were obtain from sections with varying thicknesses, but

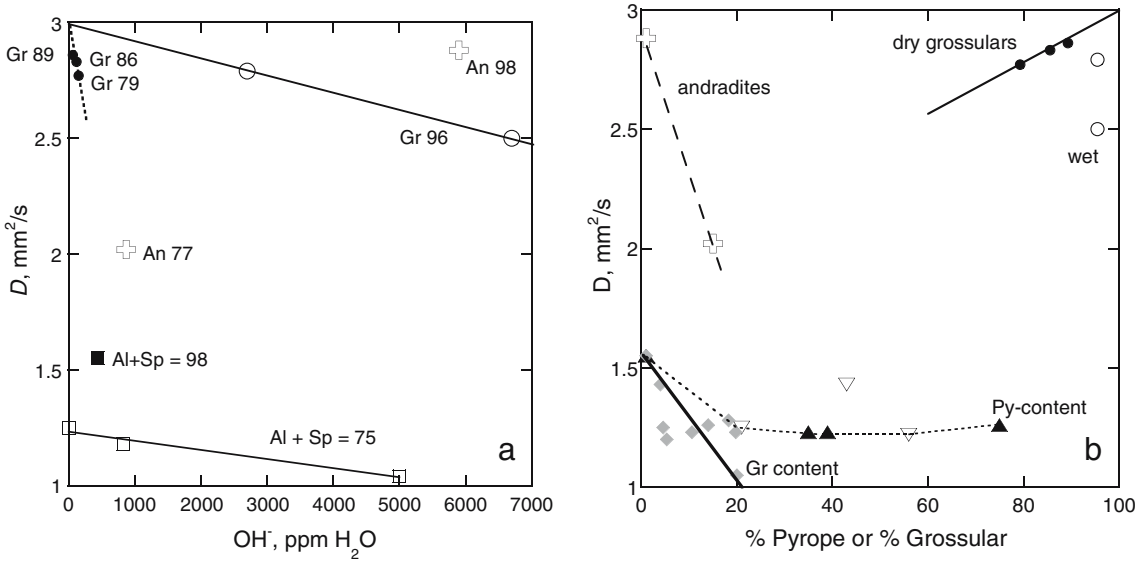

Fig. 4 Thermal diffusivity and chemical composition. **a** Hydroxyl content. *Circles* grossular-rich samples. *Squares* almandine-spessartines. Linear regressions are shown for samples with highly similar major element chemistry. *Plus sign* andradites. **b** Major element content. *Circles* $Ca_3Fe_2Si_4O_{12}$–$Ca_3Al_2Si_4O_{12}$ series; *open* indicates samples with >800 ppm H_2O. *Triangles* garnets with high $Mg_3Al_2Si_4O_{12}$ plotted against Py content; *filled* indicates samples close to the $Mg_3Al_2Si_4O_{12}$–$Fe_3Al_2Si_4O_{12}$ binary. *Gray diamonds* all pyrope–almandine–spessartines plotted against grossular content

upon heating the temperature–time curves slightly, but increasingly, departed from model curves. Only D at 298 K is reported for our small samples. Lateral dimensions of 6 mm (e.g., Mn-rich Gr) or more are needed to produce reproducible data at all temperatures.

Radiative transfer in strongly absorbing samples

For both SmGG samples, the trends in D are flatter than those of the other synthetic garnets (Fig. 3a), whether or not a metal coating was used. The temperature–time curves above 1,000 K show increasing departures from the model fit shortly after the laser pulse, similar to behavior in Fig. 2b. The flattening appears to be a milder version of strong radiative transfer that created upturns in $D(T)$ obtained using contact methods (gray curves in Fig. 3c). SmGG strongly absorbs in the near-IR, especially from 6,000 to 9,000 cm^{-1} (Fig. 1d). Strong absorptions exist for NdGG as well, and its low temperature trend is relatively shallow (Fig. 3a). At 750 K, the blackbody curve peaks at 2,600 cm^{-1} and has significant intensity to 6,500 cm^{-1}. I suggest that the shift of the blackbody curve deeper into the strongly absorbing region of 6,000–9,000 cm^{-1} as temperature increases enhances radiative transfer inside these particular chemical compositions.

Effect of hydroxyl and cation substitutions

Two disks of single-crystal grossular (wet and dry) prepared from the same sample have different D values (Fig. 3b, Table 2). The difference is ascribed to water content (Fig. 4a). Two nearly binary samples (Gr–An and Mn-rich Gr), which are very dry (Table 2), lie close to or above the trend defined by the dry grossular (Fig. 3b). Because cation disorder reduces thermal conductivity and diffusivity (e.g., Horai 1971; Giesting and Hofmeister 2002), samples with greater degrees of cation substitution should have lower D than end-member grossular. The opposite occurs, suggesting that D is also altered by the disorder which accompanies protonation. From Fig. 4a, substitution of ~0.5 wt% H_2O (which is ~10 mol% H_2O) decreases D by 25%. Decreasing the Gr content by 10 mol% decreases D by 7%, whereas decreasing the Al + Sp content by 23 mol% reduces D by 19% (Fig. 4a, Table 2). Roughly, the hydrogarnet substitution has the same effect on D as any other ion exchange, on a mole percent basis.

IR spectra of lattice modes in almandine and spessartine end-members are almost identical (Hofmeister and Chopelas 1991) suggesting that under some circumstances, Fe^{2+} and Mn garnets can be assumed equivalent. For the subset of garnets with Al + Sp = 75%, D linearly depends on OH^- content, and this trend is almost parallel to the trend for the grossulars (Fig. 4a). The sample with Al + Sp = 98% does not fall on the 75% line, consistent with grouping almandine and spessartine together, separate from the other garnet components.

Cation exchange lowers thermal diffusivity from end-member values (Fig. 4b). For essentially binary samples with similar OH^- content (dry grossulars, Table 2), the trend is linear. Both this trend and Fig. 4a predict that dry near-end member grossular has $D = 3.0$ mm^2/s. A minimum in D should exist in the middle of the grossular–andradite binary, but because our andradites are much wetter than the grossulars, the trends do not link

Table 3 Run conditions and fits to $D(T)$

Sample	Runs	L (mm)	Range[b] (K)	D_{sat} (mm^2/s)	T_{sat} (K)	Fit of $1/D$ vs T (Fig. 6, Eq. 10) (s/mm^2)	Fit range (K)
Xenocryst[f,g]	1	1.167	290–833	–	–	$0.0079486-0.0000224T+0.0266T^2\times10^{-6}-0.11284T^3\times10^{-10}$	290–833
Rhodolite[a]	1	1.83	c	c	c	$0.17509+0.0025795T-1.3874T^2\times10^{-6}$	290–875
Py–Al[a]	5	1.025	290–1,300	0.695	1,150–1,350	$-0.097321+0.0034104T-2.6156T^2\times10^{-6}+6.8585T^3\times10^{-10}$	290–1,102
Ternary	1	1.24	d	0.647	1,070–1,300	$0.252+0.0022623T-0.93052T^2\times10^{-6}$	290–1,055
Ant Hill[a]	2	1.242	290–1,300	0.661	1,150–1,300	$0.049403+0.0032299T-2.3992T^2\times10^{-6}+6.0168T^3\times10^{-10}$	290–1,105
Al–Gr	1	0.622	c	c	c	$0.19392+0.0025239T$	290–470
Al-Py	2	1.606	290–470	0.496	1,100–1,250	$0.1618+0.0025528T-1.0997T^2\times10^{-6}$	290–667
Al–Sp[a]	1	0.836	Melted	-	-	$-0.034986+0.0026544T-1.1418T^2\times10^{-6}$	290–1,015
Sp-rich	1	1.62	Melted	0.629	900–1,350	$0.082493+0.0030163T-1.4673T^2\times10^{-6}$	290–778
Grossular[a]	2	1.429	290–620	0.89	1,250–1,400	$-0.10641+0.0017914T-0.64912T^2\times10^{-6}$	290–1,360
Gr wet	2	1.41	290–1,300	-	-	$-0.068626+0.0019193T-0.72198T^2\times10^{-6}$	290–1,280
Gr–Mn[f]	2	1.2	288–1,280	<0.98	$>1,300$	$-0.042817+0.0014385T-0.44683T^2\times10^{-6}$	288–1,280
Gr–An	3	1.391	290–1,273	~0.85	-	$-0.13535+0.0018785T-0.64851T^2\times10^{-6}$	290–1,262
Gr-An2[f,g]	1	1.617	290–1,222	1.04	1,170–1,360	$-0.056641+0.0014807T-0.53542T^2\times10^{-6}$	290–1,170
An–Gr	1	1.035	290–390[c]	c	c	$-0.074145+0.0019121T$	290–390
Andradite	3	1.85	290–573	0.93	1,100–1,273	$-0.26309+0.0024971T-1.4377T^2\times10^{-6}$	290–573
YAG[a]	5	2.295,1.27	290–1573	0.762	1,350–1,600	$-0.24248+0.0017676T-0.48095T^2\times10^{-6}$	290–1,600
YIG[a]	1	1.983	290–556	0.72	~900	e	290–480
NdGG[f,,g]	1	0.888	290–480	–	–	$0.000021291+0.0011604/T$	290–480
SmGG[g]	2	1.598	290–1,440	0.82	1,200–1,420	$-0.0081448+0.0017225T-0.5555T^2\times10^{-6}$	290–1,170
SmGG:Fe[g]	1	1.233	290–1,370	0.73	1,200–1,400	$0.012658+0.0017439T-0.50313T^2\times10^{-6}$	290–1,370
EuGG:Cr	3	1.323	290–1,273	0.69	1,300–1,400	$-0.2499+0.0023147T-0.74392T^2\times10^{-6}$	290–1,270
GGG[a]	3	1.254	290–1,250	0.623	1,200–1,450	$-0.17806+0.0026027T-0.92472T^2\times10^{-6}$	290–1,257

Note All fits have correlation coefficients better than 0.99, indicating that the errors in the coefficients are small

[a]Single-crystals, although the rhodolite is fractured

[b]Temperature range deemed trustworthy, as confirmed by equivalence of data from multiple runs or during heating and cooling portions of a single run. "Melted" implies that the heating portion of the first and only run was terminated upon melting

[c]Problems with fracturing, only low T data reported

[d]D upon cooling is slightly (~5%) lower: only heating portion reported, and the highest temperature datum was omitted

[e]Ferromagnetic phase transition precludes fitting the data

[f]Small sample, results less accurate than ±2% above ~700 K

[g]Carbon-coated only: affected by radiative transfer above ~400 K (above ~550 K for the darker red xenocryst and slightly cloudy Gr–An2

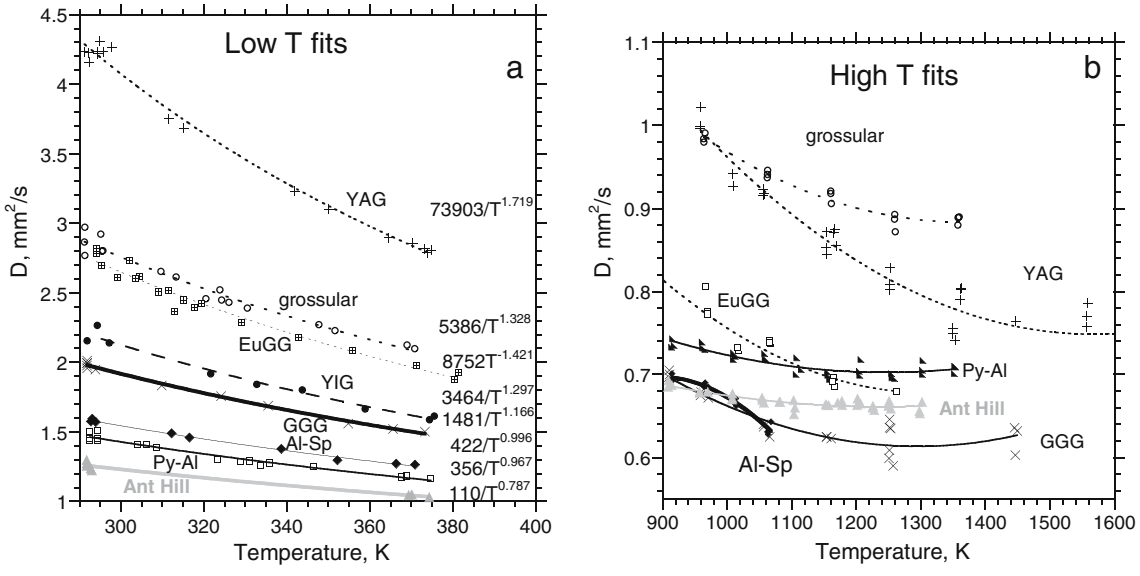

Fig. 5 Expanded views of the dependence of thermal diffusivity on temperature for single-crystals and Ant Hill garnet. *Different symbols* are used in parts **a** and **b** for clarity. **a** Low-T. Power law fits are shown in the same order as the samples. *Solid lines* indicate datasets that could be fit with a linear dependence on T. Greater curvature is associated with higher ambient temperature values for D. **b** High-T. For all samples except Al-Sp, D asymptotes to a constant. The run for Al–Sp was terminated by melting

up. A minimum is observed near the middle of the pyrope–almandine binary (Fig. 4b), but the trend is poorly constrained as our samples have Ca and Mn as well as Fe substituting for Mg (Table 1). Irregularities in the pyrope–almandine–spessartine trend are attributed to varying Ca content, because D of these samples roughly correlates with their grossular content (Fig. 4b, diamonds). This trend also is irregular because Mg is not differentiated from Mn and Fe in this projection. The large Ca ion distorts the Si–tetrahedron through edge-sharing, and thus its incorporation creates disorder in the pyrope–almandine–spessartines, much as does the hydroxyl substitution in grossular–andradites, which expands the tetrahedron via charge repulsion (e.g., Meagher 1982).

Functional dependence of thermal diffusivity on temperature

For most samples, fitting D to a polynomial in T (Fig. 3) requires high orders, e.g., 4–8, and the fit is often imperfect. Good fits with low polynomial order are obtained only over a narrow range of temperatures, e.g., below ~500 K. This type of fit is not expected to extrapolate to high temperature. Clearly, polynomial representations such as $D = \mathrm{a} + \mathrm{b}T + \mathrm{c}T^2 + \mathrm{d}T^3$ inadequately describe the vibrational heat transport.

Therefore, $D(T)$ was fit with several alternate functions, mainly those listed in the Theory section, to ascertain the best functional representation. Results from large, single-crystals (Table 3) are the focus because these data are the most accurate.

At the lowest temperatures studied, D depends linearly neither on T nor on $1/T$. Data below 400 K can be described by Eq. 6, $D = \mathrm{B}/T^{\mathrm{n}}$ if the exponent takes on values larger than unity (Fig. 5). The exponent n correlates strongly with the constant B (shown in Fig. 5a), and with the ambient temperature value (D_{298}, listed in Table 2), although the synthetic garnets (with trivalent cations in the tetrahedral sites) have steeper trends than the natural garnets (with Si^{4+} in the tetrahedral sites). In addition, for each sample, a power law is valid only up to a certain temperature which correlates inversely with D_{298}. For example, Al–Py can be fit to a power law from ~280 to 1,000 K (Fig. 3d), but YAG data diverge from a power law by 500 K. This behavior is a consequence of n, which describes the degree of curvature, correlating with D_{298}. Over the wide temperature range of our measurements, power laws (such as Eq. 3) poorly fit the data.

At the highest temperatures reached, D asymptotes to a constant value for most samples (Figs. 3, 5b). Some samples have a wide temperature range where $D(T)$ is flat (e.g., pyrope garnets and GGG): for these compositions the melting temperature is fairly high, and D_{298} is low. Conversely, samples with high D_{298} have a narrow range where D is independent of T (e.g., YAG and grossular). For samples with both low melting temperature and high D_{298} (Al–Sp), independence of D from temperature was not observed simply because sufficiently high temperatures where this behavior occurs could not be reached. Asymptotic behavior of D at high T is intrinsic, and occurs above ~1,200 K for natural garnets (Table 3, Figs. 3, 5). Fits are made at temperatures below the region of saturation.

Thermal diffusivity can be fit to $D = \mathrm{a} + \mathrm{b}/T$ only over a limited temperature range, ~290 to <800 K. Equation 7, $D = \mathrm{a}/(\mathrm{b} + T)$, did not provide a good fit, nor did Eqs. 4 to 8. The form

$$D = A + \frac{B}{T} + \frac{C}{T^2}, \tag{16}$$

which is Eq. 5 plus a constant, fit the data reasonably well for all samples, except that YAG data need an additional term ($1/T^3$).

The most accurate representation of the data is Eq. 10 wherein inverse thermal diffusivity ($1/D$) is represented by a polynomial in T up to T_{sat} (Fig. 6). For YAG, a higher order term (T^3) may be needed, but constraining this fit requires reaching higher temperatures, which are precluded by a chemical reaction near 1,600 K. Figure 6 shows that the trend in $1/D$ with temperature, particularly the region where $1/D$ asymptotically approaches a constant, largely depends on chemical composition. Curves for the synthetic garnets are nearly parallel, those of calcic garnets differ little, the bend in $1/D(T)$ of pyrope garnets occurs at essentially the same temperature, and almandines melt before the asymptotic region is reached. Fitting parameters are consistent except for SmGG which has some radiative transfer (Table 3): "A" ranges from -0.26 to $+0.25$ s/mm^2, whereas "B" ranges from 0.0018 to 0.0034 s/mm^2-K, and "C" ranges from -0.48×10^{-6} to -2.6×10^{-6} s/mm^2-K^2. Parameters are correlated with D at 298 K, which is largely governed by chemical composition (Table 3, Fig. 6). Coefficients for the cubic fits are somewhat larger. Fits to data with larger uncertainties (e.g., andradite and both SmGG samples) yielded coefficients consistent with the other garnets, unlike fitting to Eq 16.

Discussion

Comparison with previous measurements

Previous determinations of D involve pyrope–almandines and synthetic garnets. These types have insignificant OH^- contents, so cation substitution should be the sole cause of variance in D.

Ambient values determined by Kanamori et al. (1968) using the modified Ångstrom method are much lower than D determined at 298 K here for crystals of similar composition, and the trends of D with temperature are shallow, not steep (Table. 1, 2; Fig. 3c). Their reported indices of refraction and densities are not consistent with the reported compositions, and suggest significant substitution of Ca (see Giesting and Hofmeister 2002). Lower D at 298 K compared to our results on Py–Al is,

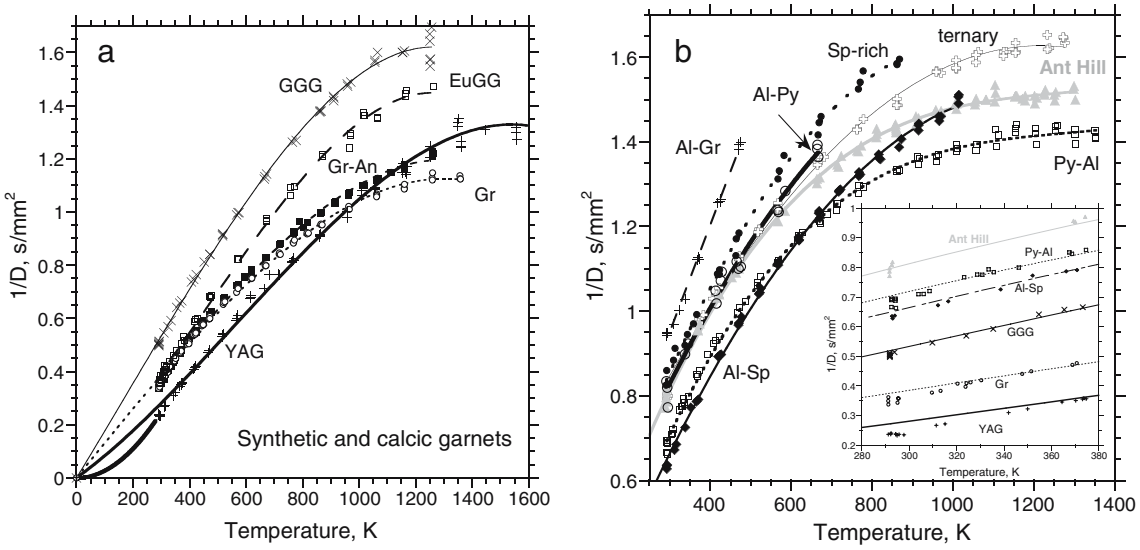

Fig. 6 Reciprocal of thermal diffusivity as a function of temperature. *Symbols* are labeled using the abbreviations in Table 1. Uncertainties are smaller than the symbols, see text. Fits are listed in Table 3. **a** Synthetic and calcic garnets. Except for Gr–An, samples are flawless single-crystals. **b** Pyrope-rich and almandine garnets. Py–Al (*squares*) and Al–Sp (*diamonds*) are single-crystals. For GGG, YAG, Gr, Ant Hill, and Al–Sp, the fits shown are of form $1/D = eT + fT^2 + gT^3$ assuming that $1/D = 0$ at $T = 0$ K. At low T, the linear trends shown do not correctly model the ambient temperature data: as shown in the inset, the measurements fall below the trends for all except mantle garnet with high values of $1/D$. The form $1/D = hT^3$ is shown, with the constant $h = 9.1\times10^9$ s/mm^2-K chosen to merge with the trend for YAG at ambient temperature

therefore, expected but the previous results are 10% below D of our ternary pyrope-rich samples as well. The positive slope for $\partial D/\partial T$ above 700 K (Fig. 3c) results from direct radiative transfer within these two single-crystals. A possible origin for the disparity at lower temperature is discussed below.

Mantle garnet ($Py_{34}Al_{57}Sp_1Gr_8$) measured by Osako (1997) using an Ångstrom technique has a composition like that of our ternary sample, but with a thermal diffusivity that is 5% lower (Table 2). The temperature dependence is not shown in Fig. 3c, because the curve is very close to that of our ternary sample up to 800 K. Agreement is excellent, given experimental uncertainties (nominally 5% for contact methods: <2% for laser flash).

Osaka et al. (2004) applied a pulse heating method to almandine with the same composition as our Al–Py sample. Their curve for $D(T)$ at pressures of 8.3 GPa is parallel to our results (Fig. 3d). The value at ambient pressure and temperature was obtained by extrapolation. Their tabulated data, which lists 1.19 mm^2/s, are in good agreement with present results.

Thermal diffusivity at 298 K of single-crystal $Py_{51}Al_{32}Sp_1Gr_{16}$ determined using picosecond transient grating spectroscopy (Chai et al. 1996) is 14% lower than D observed for our xenocryst, Ant Hill and ternary samples, which not only have appropriate Ca contents, but also have Mg contents which bracket that of Chai et al's. (1996) sample (Fig. 3c, Table. 1, 2).

Thermal diffusivity was measured at 298 K for YIG using a photothermal technique (Bertollotti et al. 1988). Their result (7.1 mm^2/s) is inconsistent with all available data on garnets. Petrunin et al. (1989) obtained $D\sim50$% higher than our measurements for gallium garnets.

Thermal conductivity has been measured at 298 K for several natural garnets by various methods (Table 2). Horai (1971) did not determine chemical compositions, but comparison can be made between samples in both studies that originated from the same locality. Linear interpolations of ρ and C_P between end-member garnets (after Giesting and Hofmeister 2002) were used to obtain k from our measurements (Table 2). Previous measurements of k at 298 K differ from our values by $\sim$14%. This discrepancy is compatible with the spread among literature values of k for each of the synthetic garnets (Table 2), and with 20–30% accuracy for contact methods (e.g., Ross et al. 1984). Additional studies cited by Giesting and Hofmeister (2002) reported neither composition nor locality; so, reasonable comparisons cannot be made.

Disparities in k at 298 K of 3–14% are associated with samples having low OH^- content. In contrast, for grossular–andradites, disparities are immense (up to 44%, Table 2). This difference is due to widely ranging concentrations of hydroxyl in Gr–An samples (e.g., Fig. 4). Not only is this quantity unknown for all previously measured samples, but major element chemistry was not determined by Horai (1971), and was estimated based on locality in Table 2. Better correspondence is obtained with the "hessonite" of Slack and Oliver (1971), probably because such material generally has low water content and is close to grossular composition.

Comparison of the temperature dependence of D with theory

Mismatch with acoustic models at moderate and high temperature

The observed non-linear decrease in D with temperature (Fig. 3) is not consistent with acoustic models (Eqs. 3, 4, 5, 6, 7, 8). Eucken's $1/T$ law (Eq. 3) is not followed above the Debye temperature as assumed in the derivation, although this law depicts some of the data over a narrow temperature range above 298 K and D for SmGG, which is affected by radiative transfer. The power law derived for solid solutions (Eq. 6) is a better match near 298 K than Eucken's law for both end-members and disordered solids, but this only holds at low temperature, in contrast to the assumptions, and for values of n larger than stipulated. For most samples, asymptotic values are reached before melting occurs, in contrast to the deduction of Roufosse and Klemens (1974). Clearly, some aspects of acoustic models describe the data, but the conditions under which the predicted functional forms fit the data are inconsistent with assumptions.

The damped harmonic oscillator model and moderate temperature behavior

Thermal diffusivity values obtained over the wide temperature range examined here are consistent with the DHO model (Eq. 10). Spectroscopic data are insufficient to examine this relationship in detail, although our measurements (Figs. 3, 5, 6) show that the FWHM controls the temperature dependence of D insofar as u depends weakly on temperature (e.g. Anderson and Isaak 1995). On this basis, Hofmeister (1999) fit $k(T)$ at low temperature to the product of a power law and an exponential function that accounted for changes in u, C_P and ρ with volume. The power law dominated the exponential component, consistent with the present fits to low temperature measurements of D. However, over our extended temperature range, a power law is not followed for $D(T)$ and is not expected for its more complicated relative $k(T)$.

Equation 10, derived from the DHO model, gives consistent results even for a limited temperature range and even if uncertainties are somewhat larger than $\pm 2\%$ attainable with large (>6 mm) single-crystals and well-formed polycrystals. This result points to $1/D$ being the best representation of heat transport.

The high temperature asymptote

Achievement of constant $1/D$ (or equivalently, constant D) at high T is largely due to the IR peak widths becoming independent of temperature. In the kinetic theory of gases, lifetimes are connected with the number of molecules per unit volume (e.g., Reif 1965). At 298 K, the FWHM of diverse crystalline structures appears to be connected with the number of phonons within the primitive unit cell (Hofmeister 2004c). As temperature increases, overtone-combination modes are excited, but saturation in the number of modes occurs when T is high enough that the continuum dominates the statistics (see Mitra 1969), and increasing T no longer significantly changes the number of phonons. The flat trend in D at high T occurs at appropriate temperatures and is consistent with saturation. Existence of an asymptotic value also mimics the Dulong–Petit law whereby heat capacity asymptotically approaches 3R (the gas constant) above the Debye temperature. We have shown here that $1/D$, and thus $k_{\mathrm{lat}}(T)$ are independent of T at roughly double the Debye temperature, and attribute this behavior to saturation of overtone-combination phonon densities, consistent with statistical thermodynamics.

Low temperature extrapolation

Values of the constant term in the polynomial fit to $1/D$ (Eq. 15) being close to and bracketing zero (Table 3) support theoretical arguments for $1/D \rightarrow 0$ in the limit of $T \rightarrow 0$ K. To explore this further, the point $1/D = 0$ at $T = 0$ was included in fitting the data. As shown in Fig. 6, a linear trend exists at low T for Ant Hill garnet which has high $1/D$ values and few data near 298 K, but for the other samples, linear trends do not quite correctly model $1/D$ near ambient temperature. Divergence of $\partial(1/D)/\partial T$ from a constant at low T clearly increases as $1/D$ decreases (Fig. 6b, inset). This behavior is consistent with forms such as $1/D = \mathrm{A}T^3$ or $1/D = \mathrm{B}T^2$ at low T for the end-members. Matching the measurements of D and the slope $\partial(1/D)/\partial T$ at 298 K approximates the behavior at cryogenic temperatures for YAG with either $A = 9.1\times10^{-9}$ s/mm^2-K^3 (shown in Fig. 6) or $B = 2.75\times10^{-6}$ s/mm^2-K^2 whereas for grossular, $B = 4\times10^{-6}$ s/mm^2-K^2 gives a better fit. For the other samples, $1/D$ almost linearly depends on T, but data below ambient temperature are needed to constrain the low temperature trends.

Extrapolation of the data to cryogenic temperatures requires that the constant term in Eq. 10 should be zero to obtain a reasonable limiting value at low T, but this approach provides a misfit near room temperature. I conclude that just as a threshold temperature exists above which Eq. 10 is invalid, so does a lower threshold temperature exist below which Eq. 10 is invalid. The lower threshold is of the order of 200 K, based on the results in Fig. 6. In the framework of the DHO model, cryogenic temperatures are dominated by depopulated optical states and thus by interactions of the acoustic modes. Therefore, theories for k and D that are based on acoustic modes should reasonably represent the data at cryogenic temperatures. For glasses, this seems to be the case as contact free measurements provide $k \sim T^2$ (Hao et al. 2004), and thus $1/D \sim T$. For crystalline solids, additional, accurate measurements at cryogenic temperatures are needed.

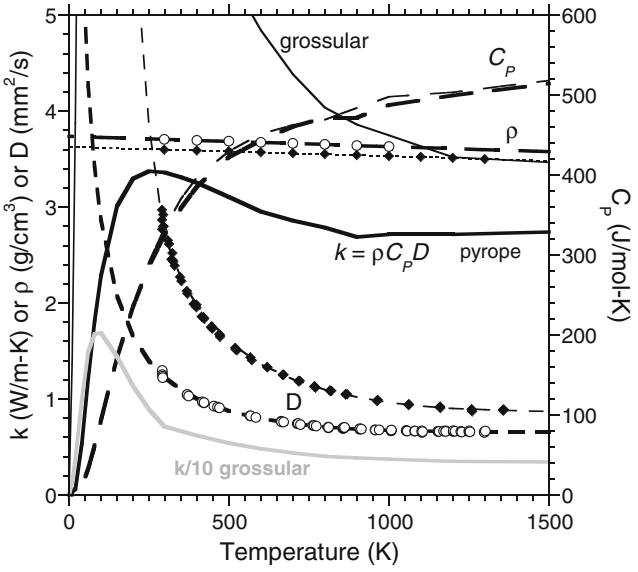

Fig. 7 Calculation of $k(T)$ from $\rho(T)C_P(T)D(T)$ for grossular- (*diamonds* and *light lines*) and pyrope-rich mantle (*circles and heavy lines*) garnets. Symbols are the data, lines are the fits, except that symbols are not shown for C_P due to the proximity of the two curves. Below 350 K, C_P data from Haselton and Westrum (1980). Grossular C_P from 350 to 1,000 K from Krupka et al. (1979); pyrope C_P from 350 to 1,300 K from Tequi et al. (1991). Densities from Anderson and Isaak (1995). The peak in $k(T)$ is caused by the opposing trends of $D(T)$ and $C_P(T)$ and that C_P approaches 0 more rapidly than does D as T decreases

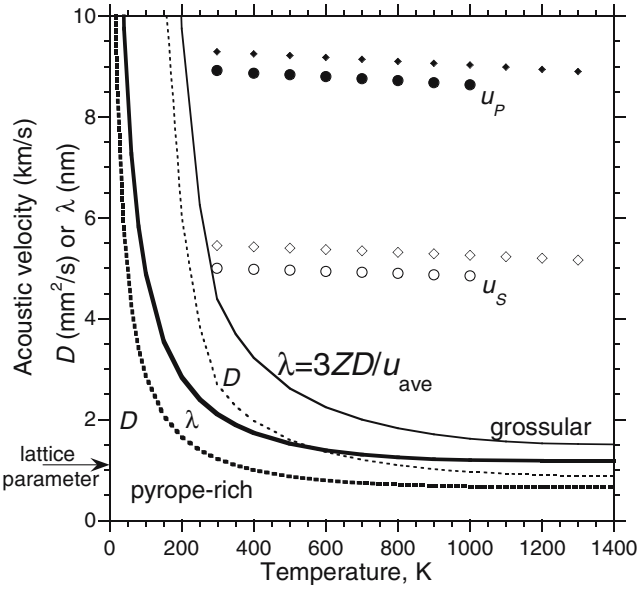

Fig. 8 Calculation of the mean free path of phonons from $u_{ave}(T)$ and $D(T)$ for grossular (*diamonds and light lines*) and pyrope-rich Ant Hill (*circles and heavy lines*) garnets. Symbols are the data, lines are the fits. At cryogenic temperatures for mantle garnet, $1/D$ was modeled as linear on T, whereas for grossular, a T^2 approximation for $1/D$ was used. Acoustic velocities were used to compute $u_{ave} = (u_P + u_S)/2$ from Anderson and Isaak (1995)

Overall behavior of $D(T)$ with implications for $k(T)$

For lattice thermal diffusity, a high threshold temperature demarcates two regimes, one strongly depending on T, the other with an asymptotically flattening value (Figs. 3, 5, 6), analogous to the Dulong–Petit limit reached in heat capacity at high T. A low threshold temperature appears to divide the strongly T-dependent regime at moderate temperatures (~250 to ~1,200 K) from the cryogenic regime. An obvious analogy exists with heat capacity, which is dominated by the behavior of acoustic modes at low temperature, optic modes at high temperature, and the Dulong–Petit limit at very high temperature. The change in $C_P(T)$ results from populations of vibrational levels changing with temperature. The possibility of interaction (phonon–phonon scattering, described by FWHM) concomitantly increases with population of the levels. Therefore, $1/D$, which is proportional to FWHM, has temperature dependence like that of C_P.

The functional form for $1/D$ has implications for $k(T)$. Figure 7 compares transport and thermodynamic functions for grossular and Ant Hill garnet: other garnets will behave similarly. At low T, we used the T^2 form for $1/D$ of grossular, but a linear dependence for Ant Hill garnet. Because D and ρ are lower order in T than is C_P, heat capacity dominates k in the cryogenic regime. For all insulators, thermal conductivity peaks below room temperature [inferred to be at 100 K for grossular and 250 K for pyrope by extrapolating our data, and

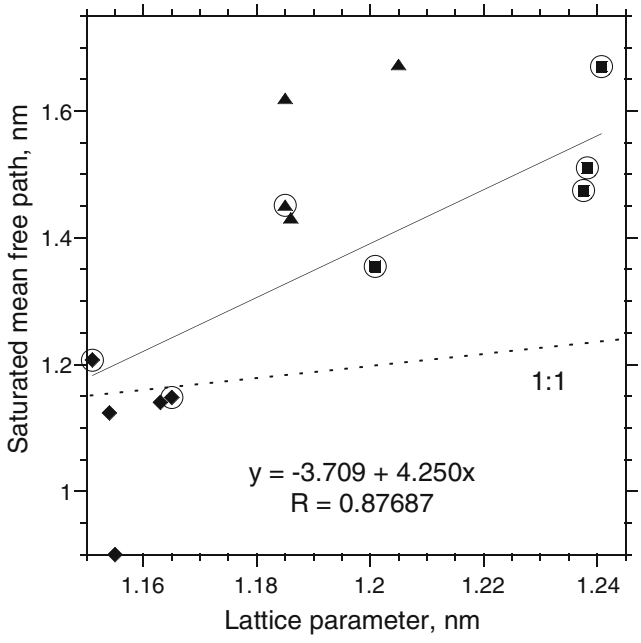

Fig. 9 Dependence of the asymptotic value of mean free path (computed from Eq. 9) on the lattice parameter of the primitive unit cell. Lattice parameters were interpolated from end-member values summarized by Smyth and McCormick (1995) or listed by Slack and Olivier (1971) or Haussühl et al. (1976) Acoustic velocities, $< u > = (u_P + 2u_S)/3$, taken from the compilations of Geisting and Hofmeister (2002) Bass (1995), and Haussühl et al. (1976). The asymptotic value of D is from Table 3. *Solid line*, least squares fit to the single-crystal data (*circles*). The fit has a correlation coefficient as indicated. *Triangles* grossular–andradites. *Squares* synthetic garnets. *Diamonds* pyrope–almandine–spessartines

observed at 20–30 K in measurements of diverse natural and synthetic garnets by Slack and Oliver (1971)] because the product $\rho C_P D$ has a peak near room temperature or below it. Above room temperature, k decreases as T increases and asymptotically approaches a constant value at high temperature. The distinct behavior of k for different temperature regions (Fig. 7) results from combining $1/D$ and C_P, both of which are complex functions of temperature (see Fig. 6; Haselton and Westrum 1980; Tequi et al. 1991). Both $1/D$ and C_P each have two threshold temperatures and different asymptotic behavior at the extremes of temperature. Because the behavior of $1/D$ and C_P with T is a response to changing populations of the various types of vibrational states with temperature, the complex form for k has the same origin. It seems unnecessary to describe k at different temperatures in terms of normal versus umklapp processes (e.g., Ziman 1962).

Mean free phonon path

The mean free path of the phonons was obtained using Eq. 9, the present results for $D(T)$, and a simple average of the compression and shear sound speeds (Figs. 8, 9). Because acoustic velocities depend linearly and weakly on temperature, $\lambda(T)$ essentially parallels $D(T)$, as shown for grossular which is an end-member, and for Ant Hill garnets, which has extensive solid solution. Other garnets will behave similarly. The mean free path approaches the lattice parameter at high temperature, which has been considered to a lower limit for λ (Ziman 1962). At low temperature, λ increases strongly as T decreases, reaching ~35 nm at 1 K for Ant Hill garnet, and a much longer mean free path of ~1 mm for grossular. If $1/D \sim T^3$, λ of pyrope-rich garnet increases to 180 mm at 1 K. Thus, only for a strong temperature dependence of D, and only for extremely low temperatures, is the mean free path long enough that phonons encounter the crystal edges before interacting with another phonon. For example, grain boundaries in ceramics (~ μm) would be encountered near 10 K for $1/D \sim T^2$. Grain boundary scattering thus is important only under restrictive conditions of ceramic textures and extremely low temperatures.

The high temperature value of λ is compared to the primitive lattice parameter for all garnets where the asymptotic limit was reached in Fig. 8. For single-crystals, λ is ~50% larger than the primitive lattice parameter. If the average speed is closer to u_S than to the weighted average of u_P and u_S used in Fig. 8, then λ more closely matches the primitive lattice parameter, but the trend for the single-crystals would still lie above the 1:1 correspondence.

Conclusions

Conventional techniques have nominal uncertainties of 5%, but are known to err by 20–30% in interlaboratory comparisons, whereas laser-flash measurements have uncertainties of ~2% and high reproducibility, as demonstrated in the materials science literature, and through comparison with standard reference materials in the present work. Comparison of the present measurements to previous data on similar garnets indicates that modern contact techniques are accurate to within 10–14%. The spectroscopic technique of Chai et al. (1996) attains the same level of accuracy as contact techniques. The laser-flash method provides the most precise values of D because this approach eliminates unwanted, direct radiative transfer effects through use of both metal coatings and the quantitative model of Mehling et al. (1998).

All garnet samples behave similarly, consistent with the oxygen sublattice dominating phonon interactions. The essential behavior consists of a strong temperature dependence for $D(T)$ between somewhat lower than ambient temperature and a critical temperature of ~1,000 to ~1,400 K, above which D is constant. At moderate temperature, heat transport is best represented as $1/D = A + BT + CT^2$. The coefficients occupy well-constrained ranges such that $A \sim 0$, B is positive and dominates the formula, and C is negative and small. The high temperature asymptote corresponds to a mean free path larger than, but similar to, the primitive lattice constant. If $1/D \rightarrow 0$ at as T $\rightarrow$ 0 K, consistent with the lack of a mechanism for exchanging heat between phonons, then $1/D$ below room temperatures going as T^n where $1 < n < 3$, and n near 2 best matches the trend near 290 K. This behavior is seen regardless of whether the chemical composition is end-member, near end-member, or extensive solid solution. Disorder and defects do not control the functional dependence of D on temperature.

Our results show that the ambient temperature values are affected by chemical composition of the end-members, and by the degree of solid solution, regardless of whether the substitution is on the anion site (OH^- replacing O^{2-} with Si^{4+} vacancies for charge balance) or on the various cation sites. Because the asymptotic values of D at high temperature are all similar for the various samples (since lattice constants vary little), the initial slope $\partial D/\partial T$, therefore, depends directly on the magnitude of D near 298 K.

The observations are consistent with the semi-empirical damped harmonic oscillator model of lattice conductivity, but not with the traditional models based on acoustic modes. However, acoustic models should reasonably represent transport at cryogenic temperatures.

Acknowledgements Support was provided by NSF EAR 0132275 and 0206121. I thank Gretchen Benedix for providing microprobe analyses.

References

Aines RD, Rossman GR (1984) The hydrous component in garnets: pyralspites. Am Mineral 69:1116–1126

Amthauer G, Rossman GR (1998) The hydrous component in andradite garnet. Am Mineral 83:835–840

Anderson OL, Isaak DG (1995) Elastic constants of mantle minerals at high temperature. In: Ahrens TJ (eds) A handbook of physical constants. American Geophysical Union, Washington DC, pp 64–96

Andre S, Degiovanni A (1995) A theoretical study of the transient coupled conduction and radiation heat transfer in glass: phonic diffusivity measurements by the flash technique. Int J Heat Transfer 38:3401–3412

Armstrong JT (1988) Bence-Albee after 20 years: review of the accuracy of α-factor correction procedures for oxide and silicate minerals. In: Newbury DE (eds) Microbeam analysis. San Francisco Press Inc, San Francisco, pp 469–476

Bass JD (1995) Elasticity of minerals, melts, and glasses. In: Ahrens TJ (eds) A handbook of physical constants. American Geophysical Union, Washington DC, pp 45–63

Bertollotti M, Fabbri L, Sibilla C, Ferrari A, Sparvieri N (1988) Photothermal deflection applied to thermal diffusivity measurements of ceramic (ferrite) materials. J Phys D Appl Phys 21:S14–S16

Blumm J, Lemarchand S (2002) Influence of test conditions on the accuracy of laser flash measurements. High Temp High Pres 34:523–528

Blumm J, Opfermann J (2002) Improvement of the mathematical modeling of flash measurements. High Temp High Pres 34:515–521

Blumm J, Henderson JB, Nilson O, Fricke J (1997) Laser flash measurement of the phononic thermal diffusivity of glasses in the presence of ballistic radiative transfer. High Temp High Pres 29:555–560

Braeuer H, Dusza L, Schulz B (1992) New laser flash equipment LFA 427. Interceram 41:489–492

Branlund J, Kameyama MC, Yuen DA, Kaneda Y (2000) Effects of temperature-dependent thermal diffusivity on shear instability in a viscoelastic zone: Implication for faster ductile faulting and earthquakes in the spinel stability field. Earth Planet Sci Lett 182:171–185

Buettner R, Zimanowski B, Blumm J, Hagermann L (1998) Thermal conductivity of a volcanic rock material (olivine–melilitite) in the temperature range between 298 and 1470 K. J Volcan Geothermal Res 80:293–302

Chai M, Brown JM, Slutsky LJ (1996) Thermal diffusivity of mantle minerals. Phys Chem Mineral 23:470–475

Cowan DR (1963) Pulse method of measuring thermal diffusivity at high temperatures. J Appl Phys 34:926–927

Debye P (1914) Vortrage über die kinetische Theorie der Materie und der Electrizität. BG Teuber, Berlin

Degiovanni A, Andre S, Maillet D (1994) Phonic conductivity measurement of a semi-transparent material. In: Tong TW (ed) Thermal conductivity 22. Technomic, Lancaster, pp 623–633

Dubuffet F, Yuen DA, Rainey ESG (2002) Controlling thermal chaos in the mantle by positive feedback from radiative thermal conductivity. Nonlin Proc Geophy 9:1–13

Ehrenberg SN (1982) Petrogenesis of garnet lherzolite and megacrystalline nodules from the Thumb, Navajo volcanic field. J Petrol 23:507–547

Eucken A (1911) Über die Temperaturabhängigkeit der Wärmeleitfähigkeit fester Nichtmetalle. Ann Phys Leipzig 34:186–221

Geiger CA, Stahl A, Rossman GR (1999) Raspberry-red grossular from Sierra de Cruces Range, Coahuila, Mexico. Eur J Mineral 11:1109–1113

Giesting PA, Hofmeister AM (2002) Thermal conductivity of disordered garnets from infrared spectroscopy. Phys Rev B65: paper #144305 (15 pages)

Gerbault M (2000) At what stress level is the central Indian Ocean lithosphere buckling? Earth Planet Sci Lett 178:165–181

Gillet P, Fiquet G, Malezieux JM, Geiger CA (1992) High-pressure and high-temperature Raman spectroscopy of end-member garnets: pyrope, grossular and andradite. Eur J Mineral 4:651–664

Hao H-Y, Newmann M, Enss C, Fleischmann A (2004) Contactless technique for thermal conductivity measurement at very low temperature. Rev Sci Instrum 75:2718–2725

Haselton HT Jr, Westrum EF Jr (1980) Low-temperature heat capacities of synthetic pyrope, grossular, and pyrope$_{60}$grossular$_{40}$. Geochim Cosmochim Acta 44:701–709

Haussühl S, Mateika D, Tolksdorf W (1976) Elasticshe und thermoelastische Konstanten von $Y_3Fe_5O_{12}$−, $Nd_3Ga_5O_{12}$−, und $Sm_3Ga_5O_{12}$−Granaten. Z Natusforsch 31:390–392

Henderson JB, Giblin F, Blumm J, Hagemann L (1998a) SRM 1460 series as a thermal diffusivity standard for laser flash instruments. Int Jour Thermophys 19:1647–1656

Henderson JB, Hagemann L, Blumm J (1998b) Development of SRM 8420 series electrolytic iron as a thermal diffusivity standard. Netzsch Applications Laboratory Thermophysical Properties Section Report No. I-9E

Höfer M, Schilling FR (2002) Heat transfer in quartz, orthoclase, and sanidine at elevated temperature. Phys Chem Mineral 29:571–584

Hofmann R, Hahn O, Raether F, Mehling H, Fricke J (1997) Determination of thermal diffusivity in diathermic materials by the laser-flash technique. High Temp High Press 29:703–710

Hofmeister AM (1999) Mantle values of thermal conductivity and the geotherm from phonon lifetimes. Science 283:1699–1706

Hofmeister AM (2001) Thermal conductivity of spinels and olivines from vibrational spectroscopy at ambient conditions. Am Mineral 86:1188–1208

Hofmeister AM (2004a) Enhancement of radiative transfer in the mantle by OH- in minerals. Phys Earth Planet Inter 146:483–485

Hofmeister AM (2004b) Thermal conductivity and thermodynamic properties from infrared spectroscopy. In: King P, Ramsey M, Swayze G (eds) Infrared spectroscopy in geochemistry, exploration geochemistry, and remote sensing. Mineralogical Association of Canada, Ottawa, pp 135–154

Hofmeister AM (2004c) Physical properties of calcium aluminates from vibrational spectroscopy. Geochim Cosmochim Acta 68:4721–4726

Hofmeister AM (2005) The dependence of radiative transfer on grain-size, temperature, and pressure: implications for mantle processes. J Geodyn 40:51–72

Hofmeister AM, Chopelas A (1991) Vibrational spectra of end-member silicate garnets. Phys Chem Minerals 17:503–526

Hofmeister AM, Campbell KR (1992) Infrared spectroscopy of yttrium aluminum, yttrium gallium, and yttrium iron garnets. J Appl Phys 72:638–646

Hofmeister AM, Fagan TJ, Campbell KM, Schaal RB (1996) Single-crystal IR spectroscopy of pyrope-almandine garnets with minor amounts of Mn and Ca. Am Mineral 81:418–428

Hofmeister AM, Schaal RB, Campbell KM, Berry SL, Fagan TJ (1998) Prevalence and origin of birefringence in 48 garnets from the pyrope–almandine–grossular–spessartine quarternary. Am Mineral 83:1293–1301

Horai K (1971) Thermal conductivity of rock-forming minerals. J Geophys Res 76:1278–1308

Kachare A, Andermann G, Brantley LR (1972) Reliability of classical dispersion analysis of LiF and MgO reflectance data. J Phys Chem Solids 33:467–475

Kanamori H, Fujii N, Mizutani H (1968) Thermal diffusivity measurement of rock-forming minerals from 300 to 1100 K. J Geophys Res 73:595–603

Klein PH, Croft WJ (1967) Thermal conductivity, diffusivity, and expansion of Y_2O_3, $Y_3Al_5O_{12}$, and LaF_3 in the range 77°–300°K. J Appl Phys 38:1603–1607

Klemens PG (1969) Theory of the thermal conductivity of solids. In: Tye RP (eds) Thermal conductivity. Academic, New York, pp 1–68

Krupka KM, Robie RA, Hemingway BS (1979) High-temperature heat capacities of corundum, periclase, anorthite, $CaAl_2Si_2O_8$ glass, muscovite, pyrophyllite, $KAlSi_3O_8$ glass, grossular, and $NaAlSi_3O_8$ glass. Am Mineral 64:86–101

Liebfried G, Schlömann E (1954) Warmleitund in elektrische isolierenden Kristallen. Nach Ges Wissenschaften Goettingen Mathematik Physik K1:71–93

McAloon BP, Hofmeister AM (1995) Single-crystal IR spectroscopy of the grossular–andradite binary. Am Mineral 80:1145–1156

Madarasz FL, Klemens PG (1987) Reduction of lattice thermal conductivity due to point defects at intermediate temperatures. Int J Thermophys 8:257–262

Maldener J, Hosch A, Langer K, Rauch F (2003) Hydrogen in some natural garnets studied by nuclear reaction analysis and vibrational spectroscopy. Phys Chem Mineral 30:337–344

Meagher EP (1982) Silicate garnets. Rev Mineral 5:25–66

Mehling H, Huatzinger G, Nilsson O, Fricke J, Hofmann R, Hahn O (1998) Thermal diffusivity of semitransparent materials determined by the laser-flash method: applying a new analytical model. Int J Thermophys 19:941–949

Mitra SS (1969) Infrared and Raman spectra due to lattice vibrations. In: Nudelman S, Mitra SS (eds) Optical properties of solids. Plenum Press, New York, pp 333–452

Osako M (1997) Thermal diffusivity of olivine and garnet single-crystals. Bull Natl Sci Mus Tokyo Ser E 20:1–7

Osako M, Ito E, Yoneda A (2004) Simultaneous measurements of thermal conductivity and thermal diffusivity for garnet and olivine under high pressure. Phys Earth Planet Int 143–144: 311–320

Padture NP, Klemens PG (1997) Low thermal conductivity in garnets. J Am Ceram Soc 80:1018–1020

Parker JW, Jenkins JR, Butler PC, Abbott GI (1961) Flash method of determining thermal diffusivity, heat capacity, and thermal conductivity. J Appl Phys 32:1679–1684

Peierls RE (1929) Zur kinetische Theorie der Warmeleitung in Kristallen. Ann der Physik Leipzig 3:1055–1101

Petrunin GI, Popov VG, Timoshechkin MI (1989) Temperature dependences of the heat capacity, diffusivity, and thermal conductivity of gallium garnets (300–700 K) (translated). Teplofisika Vysokikh Temp 27:1097–1102

Pomeranchuk I (1943) Heat conductivity of dielectrics at high temperatures. J Phys USSR 7:197–201

Reif F (1965) Fundamentals of statistical and thermal physics. McGraw Hill Book Co, New York

Ross RG, Andersson P, Sundqvist B, Bäckström G (1984) Thermal conductivity of solids and liquids under pressure. Rep Prog Phys 47:1347–1402

Rossman GR (1988) Optical spectroscopy. Rev Mineral 18:207–254

Rossman GR, Aines RD (1991) The hydrous components in garnets: grossular–hydrogrossular. Am Mineral 76:1153–1164

Roufosse MC, Klemens P G (1974) Lattice thermal conductivity of minerals at high temperatures. J Geophys Res 79:703–705

Schaal RB (1991) I. Geometric modeling in reaction space of mineralogical diversity among eclogites. II. Constraints on shallow subduction of the Farallon plate from mantle xenoliths of the Colorado Plateau. PhD dissertation, University of California, Davis, 128 pp

Schilling FR (1999) A transient technique to measure thermal diffusivity at elevated temperatures. Eur J Mineral 11:1115–1124

Seipold U (1998) Temperature dependence of thermal transport properties of crystalline rocks—a general law. Tectonophysics 291:161–171

Slack GA, Oliver DW (1971) Thermal conductivity of garnets and phonon scattering by rare-earth ions. Phys Rev B4:592–609

Smyth J, McCormick T (1995) Crystallographic data for minerals. In: Ahrens TJ (eds) A handbook of physical constants. American Geophysical Union, Washington DC, pp 1–17

Spitzer WG, Miller RC, Kleinman DA, Howarth LW (1962) Far-infrared dielectric dispersion in $BaTiO_3$, $SrTiO_3$, and TiO_2. Phys Rev 126:1710–1721

Tan HP, Maestre B, Lallemand M. (1991) Transient and steady-state combined heat transfer in semitransparent materials subjected to a pulse or step irradiation. J Heat Transfer 113:166–173

Taran MN, Langer K (2001) Electronic absorption spectra of Fe^{2+} ions in oxygen-based rock-forming minerals at temperatures between 297 and 600 K. Phys Chem Minerals 28:199–210

Tequi C, Richet P, Robie RA, Hemingway BS, Neuville DR (1991) Melting and thermodynamic properties of pyrope ($Mg_3Al_2Si_3O_{12}$). Geochim Cosmochim Acta 55:1005–1010

Van den Berg AP, Yuen DA, Rainey ESG (2004) The influence of variable viscosity on delayed cooling due to variable thermal conductivity. Phys Earth Planet Inter 142:283–295

Yanagawa TKB, Nakada M, Yuen DA (2005) The influence of lattice thermal conductivity on thermal convection with strongly temperature-dependent viscosity. Earth Space Sci 57:15

Ziman JM (1962) Electrons and phonons: the theory of transport phenomena in solids. Clarendon Press, Oxford, 550 pp (Ch 8 and 11)